Available online at www.sciencedirect.com
ScienceDirect
Journal of Power Sources 172 (2007) 324–333
JOURNAL OF POWER SOURCES
www.elsevier.com/locate/jpowsour

Thermal analysis and optimization of a portable, edge-air-cooled PEFC stack

Reto Flückiger [a,*], Andreas Tiefenauer [b], Martin Ruge [c], Christian Aebi [d], Alexander Wokaun [a], Felix N. Büchi [a]

[a] *Electrochemistry Laboratory, General Energy Research Department, Paul Scherrer Institut, CH-5232 Villigen PSI, Switzerland*
[b] *Center for Computational Physics, Zurich University of Applied Sciences, CH-8401 Winterthur, Switzerland*
[c] *Fuel Cell Laboratory, Berne University of Applied Sciences, CH-2501 Biel, Switzerland*
[d] *CEKA Elektrowerkzeuge AG, CH-9630 Wattwil, Switzerland*

Received 22 December 2006; received in revised form 3 May 2007; accepted 19 May 2007
Available online 25 May 2007

Abstract

Internally humidified, edge-air-cooled PEFC stacks are promising for portable systems in terms of specific power and specific cost. However, their main drawbacks are thermal power limitations due to limited heat removal from inside the stack. The aim of this work is to minimize the cooling limitation with a simultaneous cost and weight reduction by optimization of the stack geometry. A steady-state, thermal FE-model was developed and validated against experimental temperature distributions. The model includes anisotropic heat conduction and heat convection by the cooling air. Cell voltage, liquid water fraction and limiting temperature were experimentally determined for improved accuracy. Complex flowfield structures were approximated with the numerical volume averaging method to reduce computational cost. As a result of the optimization study specific power was improved by +86% with simultaneous reduction of specific cost by −35%.

Keywords: PEFC; Edge-air-cooling; Thermal analysis; Specific power; Specific cost

1. Introduction

It is widely recognized that the transition from prototype scale fuel cells to marketable, portable power supplies will only succeed if a significant cost reduction with a simultaneous increase in power density can be achieved. In the power range of 200 W to 2 kW, polymer electrolyte fuel cell (PEFC) systems for portable applications have a specific cost target of below 2 € W^{-1} and a specific power target of above 100 W kg^{-1} [1] in order to compete with conventional gen-sets. In 2001 Ballard introduced the Nexa® power module, an area-air-cooled, 1200 W PEFC system with a specific cost of about 5 € W^{-1} and a specific power of about 92 W kg^{-1}. Other potential low-cost, air-cooled PEFC stack concepts for portable applications have also been put forth [2–5]. The group at Siemens [4] reported a specific cost of about 2.8 € W^{-1} for their prototype-stack in 2002.

On the one side, specific cost is strongly influenced by the cost of the electrochemical components such as membrane and catalyst, but on the other side it is also strongly dependent on stack construction and system integration. Therefore a simple and cheap design and fabrication method is needed to considerably reduce cost. As the main burdens in the fuel cell system are cooling and humidification [6], the system layout can be simplified by including reactant humidification into the stack [7], and choosing air as the cooling media. At least three different arrangements of heat removal by air are possible: (i) cooling air is passed through the stack, so-called area-air-cooling [2–4]; (ii) excess process air is used as cooling air [8]; (iii) cooling air is passed on the surface of the stack, so-called edge-air-cooling. Because area-air-cooling requires a complex stack design the solutions (ii) and (iii) with only two media in the stack allow for simple and cheap designs. Cooling with excess process air can involve difficult performance stability (membrane drying), cathode contamination (high air volumes through cathode) and high air pumping power (high air volumes). Therefore the edge-air-cooling solution is the most favorable

* Correspondingauthor. Tel.: +41 563104189; fax: +41 563102199.
E-mail address: reto.flueckiger@psi.ch (F.N. Büchi).

0378-7753/$ – see front matter © 2007 Elsevier B.V. All rights reserved.
doi:10.1016/j.jpowsour.2007.05.079

air-cooling option offering constructive and operational advantages.

The development at Siemens [4] has shown the advantages, with respect to fabrication, of the "stamp and punch" approach for bipolar plates. However, with the metal substrates chosen, corrosion problems were hampering lifetime. A stack concept which combines the advantages of internal reactant humidification, "stamp and punch" approach and simple edge-air-cooling has been proposed by Ruge and Höckel [9]. They used carbon-based bipolar plates to avoid corrosion problems and ensure high thermal and electrical conductivity. The only drawback of this concept is the thermal power limitation caused by the heat removal from the stack surface only. It can be minimized by optimizing cell geometry with respect to active area size and plate thicknesses.

This challenge is tackled by means of a finite element (FE) model focusing on global heat source/sinks and transport. Starting from a base case used for model validation, optimization of the geometry with respect to watt-specific cost and weight-specific power was performed.

For a better understanding of the system we first resume the design of the prototype-stack. Then a detailed description of the model and model parameters follows. As a first result the successful model validation is presented. Finally the optimization of the specific cost and specific power is discussed.

2. Stack design

The stack design of Ruge and Höckel is based on the concepts of internal humidification [7], punching of carbon-based bipolar plates [9] and edge-air-cooling.

2.1. Bipolar plate

The bipolar plate is composed from a separator plate and two perforated plates for each flowfield. The separator plate with an unoptimized thickness of $d_{sp} = 0.55$ mm not only separates the anode and cathode gases but acts simultaneously as a cooling rib as showed in Fig. 1. It is laterally extended over the active area of the cell in order to be cooled by the cooling air massflow. Two

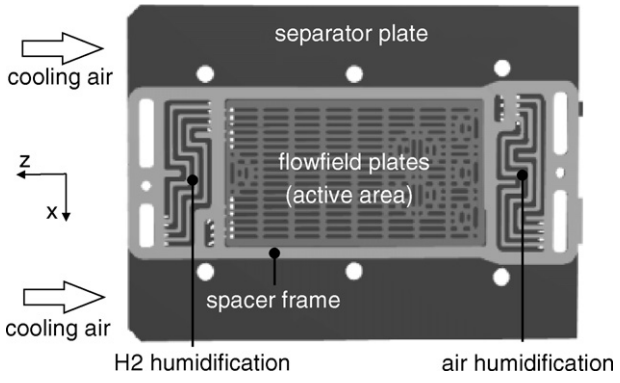

Fig. 1. Top view of an open cell with the bipolar plate (flowfield plate + separator plate) and the spacer frame with the hydrogen and air humidification flowfields. Ambient air is blown in negative z-direction over the separator plate.

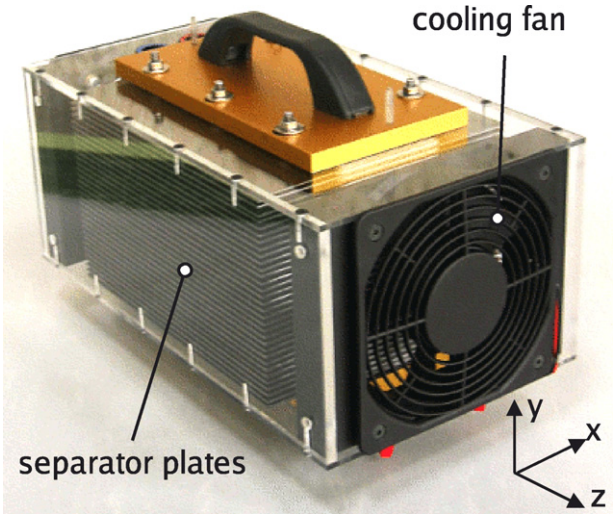

Fig. 2. Photograph of the 500 W prototype-stack with 30 cells. The separator plates are visible behind the transparent sidewall.

perforated plates with a thickness of $d_{ff} = 0.29$ mm complement one another to a continuous serpentine flowfield. The channels are staggered and rectangularly shaped with a depth of 0.58 mm and a width of 1.3 mm. Perforated plates can be made in mass production by punching at unrivaled cost. For the separator and flowfield plates SIGRAFLEX® from SGL Carbon was used. This material is a good electric ($\sigma = 16000\ \mathrm{S\ m^{-1}}$) and excellent thermal conductor ($\kappa = 290\ \mathrm{W\ m^{-1}\ K^{-1}}$) and readily available at low cost.

2.2. Cell

A cell is assembled from a bipolar plate, a membrane electrode assembly (MEA) and a spacer frame. The MEA is a pMembrain H300 from Umicore based on Nafion 112. The spacer frame ensures a homogeneous compression of the MEA and sealing. It also provides the humidification flowfields for both gases. The humidification concept is discussed in detail in [7]. The active area of a prototype cell is $A = 63\ \mathrm{cm^2}$.

2.3. Stack

The 500 W prototype-stack shown in Fig. 2 is assembled from 30 cells. For the cooling of the separator plates, a controllable fan is integrated directly into the stack, blowing cold air in negative z-direction over the separator plates. This stack configuration had a specific power of 85 $\mathrm{W\,kg^{-1}}$ and the specific cost was estimated at 3.2 € $\mathrm{W^{-1}}$ before optimization.

2.4. Cooling design

Fig. 3a shows a schematic of an area-cooled and Fig. 3b of an edge-cooled three-cell stack. In area-cooled designs, like the Ballard NEXA® module, the cooling air is distributed over the entire cell area by means of small channels. This air distribution allows for local heat removal and reduces the temperature

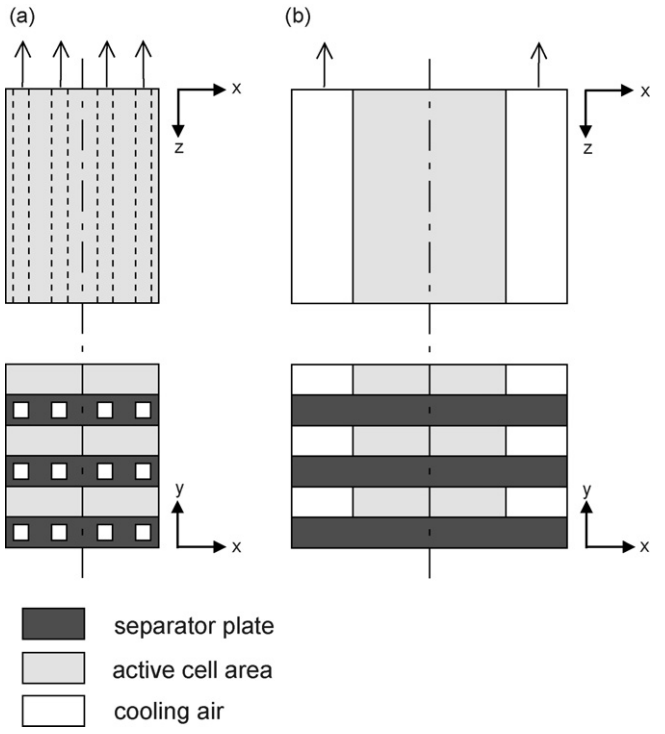

Fig. 3. Simplified schematic of the cooling design. (a) Plan and section view of an area-cooled three-cell stack. (b) Plan and section view of an edge-cooled three-cell stack.

gradients. On the other hand the stack complexity increases and the power demand of the fan grows due to significant pressure losses in the small channels. An edge-air-cooled design omits these drawbacks as cooling air is passed in wide channels along the edges of the active cell area. A negative effect of the edge-air-cooled concept is an amplification of the cooling limitation as the thermal diffusion path to the cooling air is considerably elongated.

3. Model

The model is a steady state, thermal model of a cell including the cooling air. Its main objective is the investigation of heat transport bottlenecks within edge-air-cooled cells. Due to these bottlenecks the cells have to be operated at lower current densities. Otherwise the temperature limit in the center of the cell would be exceeded. The model automatically adjusts the current density in order that the preset maximum temperature T_{limit} is not surpassed.

3.1. Assumptions

In order to have an efficient model for extensive optimization studies, the following simplifying assumptions have been made:

- steady-state conditions,
- Nernst potential and overpotentials replaced by experimental current–voltage characteristic,
- homogeneous heat source in the cathode catalyst layer,
- constant liquid water fraction in exit gases,
- no liquid water transport,
- no heat transport by process gases (7% conservative error),
- no heat transfer resistances between solid–solid boundaries,
- perfect isolation to the environment, and
- laminar cooling air.

These assumptions are explained and justified in the following. In reality reactant stoichiometry, current density, reactant pressure and cell temperature influence the thermal management of the stack. The current density has the strongest impact on the thermal management. It determines the operating point and therewith the fraction of energy transformed into heat. The model considers a variable current density. For the determination of the cell voltage a static current voltage characteristic at a given stoichiometry, pressure and temperature was used.

The influence of the temperature distribution on the cooling behavior is the main purpose of the model. However, the influence of the temperature to the reaction kinetic and the liquid water transport is not explicitly considered, but taken account of by the static current voltage characteristic. Liquid water transport is not considered as the dew point was assumed to be significantly below the cell temperature. Nevertheless the influence of liquid water on the enthalpy of formation is accounted for.

In the base case at 3880 $\mathrm{A\,m^{-2}}$, the mean heat removal by the reactant gases was estimated to be $Q = 1.1\,\mathrm{W}$ per cell at a reactant massflow of $\dot{m} = 0.0665\,\mathrm{kg\,h^{-1}}$ with a mean heat capacity of $c_\mathrm{p} = 1500\,\mathrm{J\,kg^{-1}\,K^{-1}}$ and a temperature difference of $\Delta T = 40\,^\circ\mathrm{C}$. This contribution is only 7% of the total heat removal of $Q = 16\,\mathrm{W}$ in the base case. The influence of the stoichiometry on the cooling was therefore neglected. The stoichiometry is accounted for as a constant in the current–voltage characteristic.

Higher reactant pressure reduces overpotential and therewith the heat loss. The used current–voltage characteristic was measured at a relatively low pressure of 1 bar ensuring a conservative determination of the heat loss.

3.2. Domain and geometry

The model domain and the coordinate system definition are shown in Fig. 4. The domain comprises the smallest repeat unit of a single cell which results from a bisection along the z-axis. The model distinguishes seven domains for heat transport:

- Ω_1 membrane,
- Ω_2 anode/cathode gas diffusion layers (GDL),
- Ω_3 anode/cathode flowfields,
- Ω_4 anode/cathode humidification flowfields,
- Ω_5 spacer frame,
- Ω_6 separator plate, and
- Ω_7 air channel.

To further reduce the complexity of the model geometry and to accelerate the computation we applied the numerical volume averaging method (NVAM) as described in [10]. By means of

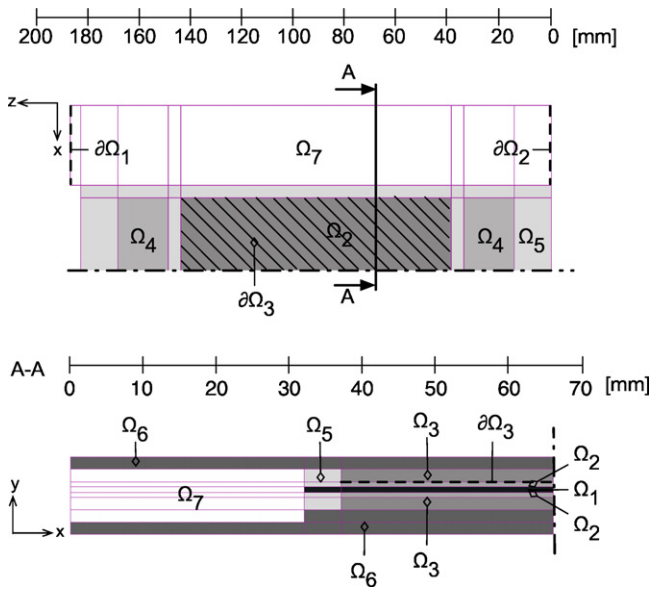

Fig. 4. Schematic horizontal (top) and vertical (bottom) sections through the model domains (figures are not to scale). Ω: domains, $\partial\Omega$: boundary conditions.

Table 1
Intrinsic and effective thermal conductivities of the flowfields

	$\kappa_{ff,x}$	$\kappa_{ff,z}$	$\kappa_{ff,y}$
Intrinsic ($W\,m^{-1}\,K^{-1}$)	290	290	12.1
Effective ($W\,m^{-1}\,K^{-1}$)	21.7	138.1	1.71

this method the meander-like structure of the flowfields Ω_3 were approximated by simple, unstructured domains. These domains incorporate the averaged, effective thermal conductivities of Table 1 that correspond to the real configuration.

The real flowfield structure was considered in a separate 3D sub-model (Fig. 5) of the smallest repeat unit of a flowfield ignoring bend geometries. The effective conductivities for every direction were determined by applying a virtual temperature difference to the sub-model. The resulting, integrated heat flux and the applied temperature difference were used with an approximation of Fick's first law to obtain the effective conductivities.

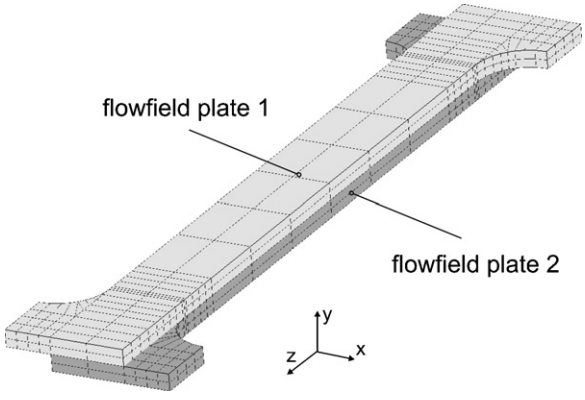

Fig. 5. Numerical volume averaging model of the flowfield. Smallest repeat unit (without bend geometry) of two staggered, perforated plates.

3.3. Governing equations

The basic physical model is described by the steady state, frictionless energy conservation law in Eq. (1). Although the transient thermal behavior is important, steady-state conditions are sufficient for the investigation of heat transport bottlenecks:

$$\nabla(h_{\text{air}}\rho_{\text{air}}\vec{v}) = D_t p - \nabla\vec{F} + q \tag{1}$$

Therein ρ_{air} is the temperature-dependent air density, h_{air} the temperature-dependent air enthalpy, $D_t p = \partial_t p + \vec{v}\nabla p$ the total time derivative of the pressure ($\partial_t p = 0$), $\vec{v}$ the air velocity determined by solving the Navier–Stokes equation, $\vec{F}$ the conductive heat flux and q is the heat source. The conductive heat flux $\vec{F}$ is given by Fick's first law in Eq. (2):

$$\vec{F} = -\kappa\nabla T \tag{2}$$

κ is the anisotropic conductivity tensor as given in Eq. (3):

$$\kappa = \begin{bmatrix} \kappa_x & 0 & 0 \\ 0 & \kappa_y & 0 \\ 0 & 0 & \kappa_z \end{bmatrix} \tag{3}$$

Anisotropic heat conduction is considered in the GDLs (Ω_2), the flowfields (Ω_3) and the separator plates (Ω_6). The other domains show an isotropic thermal behavior. Heat convection is only accounted for in the cooling air channel (Ω_7). The left hand side of Eq. (1) is zero for all solid domains including the flowfields. The heat source q is set to zero in all domains since the heat is released by means of an internal boundary condition.

3.4. Boundary conditions

The problem description was completed with boundary conditions for the unknown temperature and pressure fields. As shown in Fig. 4 there are three different boundary conditions: (i) cooling air inlet ($\partial\Omega_1$): the temperature field is set to the ambient temperature T_{amb} and the pressure field is defined to satisfy the cooling air massflow $\dot{m}_{\text{cool}}$. (ii) Cooling air outlet ($\partial\Omega_2$): the pressure is set to ambient pressure p_{amb}. (iii) Cathode catalyst layer ($\partial\Omega_3$): the normal heat flux through this internal boundary condition is increased with q as described in Eq. (4). The other boundaries are perfectly isolated, hence $\nabla T = 0$ applies. This means, that fringe effects of the endplates are not considered.

3.5. Model parameters

The model contains three sensitive parameters: (1) cell voltage as a function of current density, (2) liquid water fraction, and (3) limiting temperature. They are determined experimentally as described in the following.

3.5.1. Cell voltage

Different operating points involve different losses resulting in different heat sources. Instead of solving Laplace equation for electron conduction and implementing the overpotential models to determine the cell voltage in real time, we used the

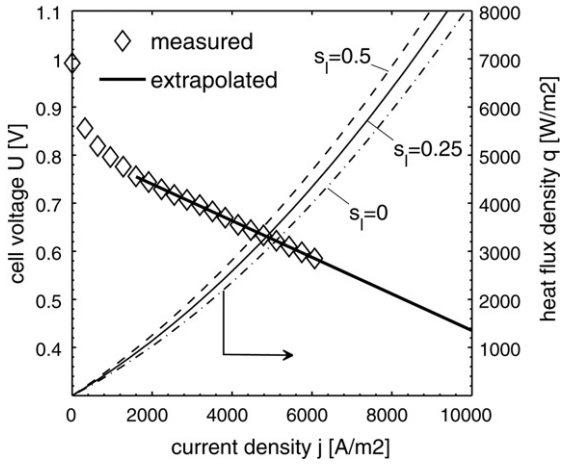

Fig. 6. Measured current–voltage characteristic and heat source as a function of liquid water fraction s_l. $\lambda_{air} = 3.3$, $\lambda_{H_2} = 1.3$; 1.0 bar anode/cathode pressure; 70 ° C mean cell temperature; and 250 h of operation.

experimental current–voltage characteristic in Fig. 6. This static current–voltage characteristic allowed for significantly shorter computation times and is justified by using the same type of MEA for the optimization study. The current–voltage characteristic was measured at a cathode/anode pressure of 1 bar, an air stoichiometry of $\lambda_{air} = 3.3$, a hydrogen stoichiometry of $\lambda_{H_2} = 1.3$, a mean cell temperature of 70 ° C and after an operation time of 250 h. This accounts for a certain degradation and ensures a conservative determination of the losses. All the studies below were performed around a mean cell temperature of 70 °C. Therefore the current–voltage characteristic of Fig. 6 is applicable. Cell voltages above 6000 A m^{-2} were extrapolated linearly. Mass transport limitations at high current densities were consciously ignored in order to investigate the thermal limitation independently.

3.5.2. Heat source distribution

The cell overvoltage and the entropy change of the electrochemical reaction are losses transformed into heat. This heat source depends on the liquid water fraction s_l and is assumed to be released in the cathode catalyst layer. Eq. (4) gives the heat production per unit area as a function of the operating point and the enthalpy of formation of water ΔH_f:

$$q = \left(\frac{\Delta H_f}{2F} - U \right) j \tag{4}$$

The current density j is normally inhomogeneous over active area of technical relevance. These inhomogeneities along the channel have been extensively investigated in the past [11]. Largely inhomogeneous current density distribution for co-flow and current densities below 6000 A m^{-2}, caused by insufficient membrane humidification, were observed. However, in the present case the following facts have an averaging effect on temperature inhomogeneities and justify the use of a homogeneous heat source in this model:

- The large thermal in-plane conductivity of the bipolar plate material ($\kappa_{sp} = 290$ W m^{-1} K^{-1}) results in small temperature gradients in the active area. Hence a high local heat production is dispersed to the total active area.
- The serpentine type, counter-flowfield has an averaging effect on the membrane humidification and the current density distribution consequently.
- The stack is operated at relatively high stoichiometries due to the staggered flowfield design. This results in small oxygen depletion and homogeneous reaction distribution along the channel.
- The long heat conduction paths to the cooling channels result in averaged global heat fluxes which are not sensitive to local temperature inhomogeneities.

Nevertheless, for validating the model, different virtual heat source profiles were investigated.

3.5.3. Liquid water fraction

ΔH_f depends on the state of the water formed by the oxygen reduction reaction:

$$\text{liquid water} : \Delta H_{f,l} = -285.8 \times 10^3 \text{ J mol}$$

$$\text{gaseous water} : \Delta H_{f,g} = -241.8 \times 10^3 \text{ J mol}$$

The heat production as a function of current density is illustrated in Fig. 6 for different liquid water fractions. To estimate the liquid water fraction, the prototype-stack was operated at a known current density j_0 and cathode massflow rate, while the cathode outlet temperature $T_{c,o}$ was measured. The gaseous water pressure was determined by assuming a fully humidified gas at $T_{c,o}$. From this the liquid water fraction s_l was determined according to Eq. (5):

$$s_l = 1 - \frac{\dot{m}_{H_2O,g}}{r_{H_2O}} j_0 \tag{5}$$

where $\dot{m}_{H_2O,g}$ is the water vapor massflow at the cathode outlet and r_{H_2O} is the total water production rate.

A constant liquid water fraction s_l was assumed as the anode/cathode pressure and the maximum cell temperature were kept constant. With the upper limit of the liquid water fraction $s_l = 0.17 \pm 0.06$ the enthalpy of formation was finally determined according to Eq. (6):

$$\Delta H_f = s_l \Delta H_{f,l} + (1 - s_l) \Delta H_{f,g} \tag{6}$$

3.5.4. Limiting temperature

The power output of a PEFC is temperature dependent. Fig. 7 shows the measured power output over temperature at three different currents. At high temperatures the membrane water content is reduced resulting in higher ohmic losses. Exceeding a critical temperature threshold, the limiting temperature T_{limit}, should be prevented. Above this temperature irreversible damages are expected.

Fig. 7 illustrates that the optimum and limiting temperature do not strongly depend on the current as the stoichiometry was kept constant. Therefore these two parameters are applicable to all the operating points with the same stoichiometries. The limiting temperature is defined at 95% of the maximum power

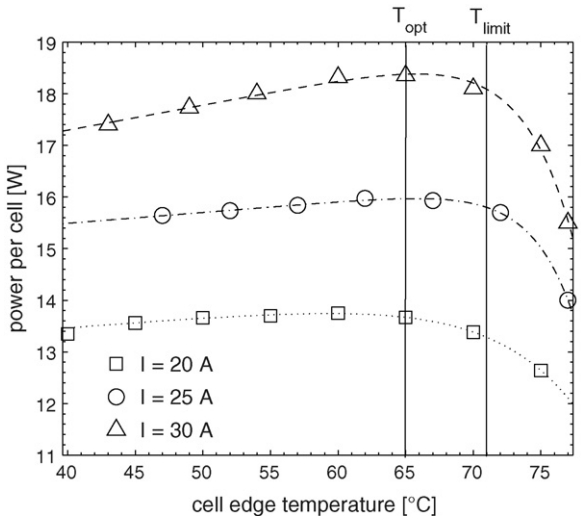

Fig. 7. Measured power output per cell as a function of cell-edge temperature for three different currents. $\lambda_{air} = 4.5$; $p_{air} = 1.0$ bar; $p_{H_2} = 1.5$ bar; and $A = 62.6\,cm^2$.

output above the optimum temperature. According to Fig. 7 the optimum temperature at the edge of the active area is around 65 ° C and the limiting temperature is around 71 °C. Knowing that the average temperature difference between the edge and the hottest point in the cell is about 4 °C, the critical temperature for this system was defined at $T_{limit} = 75$ °C.

Table 2 gives an overview of the base case model parameters. The values j, $\dot{m}_{cool}$, d_{sp}, w_{ff} and l_{ff} are optimized in terms of specific cost and weight.

Table 2
List of base case model parameters

Symbol	Description	Value
$\dot{m}_{cool}$ (kg h^{-1})	Cooling air massflow per cell	1.33
j (A m^{-2})	Current density	3880
s_l	Liquid water fraction	0.17 ± 0.06
ΔH_f (kJ mol^{-1})	Enthalpy of formation of product water	251.95
T_{limit} (°C)	Limiting temperature	75
T_{amb} (°C)	Ambient temperature	25
p_{amb} (Pa)	Ambient pressure	1e5
$\kappa_{ff,x}$ (W m^{-1} K^{-1})	Flowfield thermal x-conductivity	21.7
$\kappa_{ff,z}$ (W m^{-1} K^{-1})	Flowfield thermal z-conductivity	138.1
$\kappa_{ff,y}$ (W m^{-1} K^{-1})	Flowfield thermal y-conductivity	1.71
$\kappa_{sp,x}$ (W m^{-1} K^{-1})	Separator plate thermal x-conductivity	290
$\kappa_{sp,z}$ (W m^{-1} K^{-1})	Separator plate thermal z-conductivity	290
$\kappa_{sp,y}$ (W m^{-1} K^{-1})	Separator plate thermal y-conductivity	3.5
$\kappa_{gdl,x}$ (W m^{-1} K^{-1})	GDL thermal x-conductivity	23
$\kappa_{gdl,z}$ (W m^{-1} K^{-1})	GDL thermal z-conductivity	23
$\kappa_{gdl,y}$ (W m^{-1} K^{-1})	GDL thermal y-conductivity	1.7
κ_{fr} (W m^{-1} K^{-1})	Cell frame thermal conductivity (isotropic)	0.23
κ_{mem} (W m^{-1} K^{-1})	Membrane thermal conductivity (isotropic)	0.45
d_{fr} (mm)	Cell frame thickness	0.8
d_{mem} (mm)	Membrane thickness	0.0508
d_{ff} (mm)	Flowfield thickness	0.29
w_{ff} (mm)	Flowfield width	58
l_{ff} (mm)	Flowfield length	108
w_{sp} (mm)	Separator plate width	122
d_{sp} (mm)	Separator plate thickness	0.55

3.6. Implementation

The model was realized with the FE-based multiphysics software NMSeses [12]. Depending on the parameter-set the simulation of one operating point took 3–5 min (Pentium 4, 3.2 GHz, 1 GB RAM). For the optimization studies the maximum cell temperature was iterated to the limiting temperature. For this purpose a Perl-Script was implemented to check after every simulation whether the maximum cell temperature is above or below the limiting temperature. The current density was then adjusted according to the bisection method [13] and a new iteration was started.

4. Results and discussion

This section presents the validation procedure and the results of the optimization study. First we studied the dependency of the power output on the cooling air massflow. Then we investigated the influence of geometry on the specific cost and finally the effect of geometry on the specific power was analyzed.

4.1. Model validation

The model was validated by temperature measurements at the 500 W prototype-stack. The solid temperature of the separator plate was measured by a displaceable, Type-K thermocouple in the cooling channel ($x = 16$ mm) and at fixed points inside the flowfield ($z = 90$ mm, $z = 168$ mm). The model parameters in Table 2 used for the base case correspond to the prototype-stack. The validation was made without the artificial tuning of the maximum temperature towards the limiting temperature. The only fit parameter was the cooling air massflow. It was adjusted to the best correlation of temperature between experiment and model prediction.

4.1.1. Temperature profiles

Fig. 8a compares the temperatures profiles along two different z-lattices with the corresponding experimental data. One lattice marks the middle of the cooling channel ($x = 16$ mm) and the other denotes the symmetry line ($x = 66$ mm). The cooling air is flowing in negative z-direction from $z = 188$ mm at the air inlet to $z = 0$ mm at the air outlet. The dashed vertical lines at $z = 40$ and 148 mm define the active area where the heat is released. The predicted profiles within the active area correlate well with the measurements.

In Fig. 8b the temperature profile along the x-lattice at $z = 90$ mm is compared with experimental data accordingly. The vertical dashed lines mark the border between the active area, the sealing by the frame material and the cooled area of the separator plate. The modeled temperature profile in x-direction is also in good accordance with the experimental data which confirms the validity of the model.

4.1.2. Inhomogeneous heat source distribution

Fig. 8 comprises error ranges attributed to the homogeneous heat source assumption. The upper temperature limits are the result of an unfavorable, linear heat source profile (negative

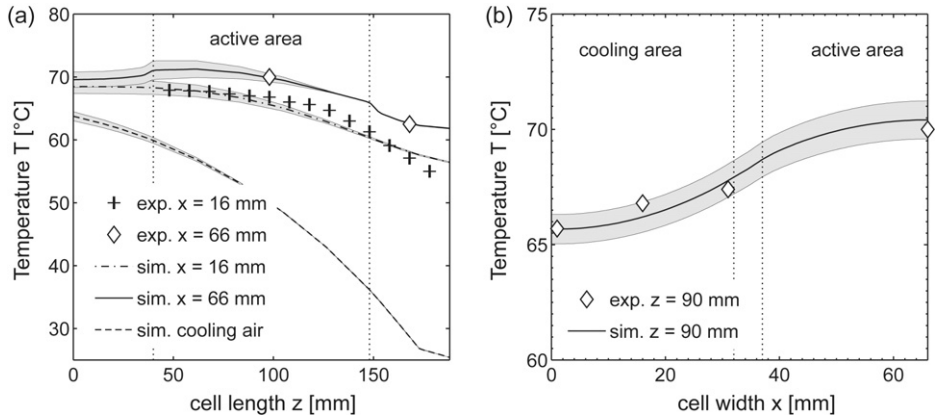

Fig. 8. Comparison of experimental and simulated temperature profiles including error ranges (gray areas) attributed to the homogeneous heat source assumption. (a) Temperature profiles along the cooling air. (b) Temperature profile perpendicular to the cooling air at $z = 90$ mm. $\dot{m}_{cool} = 1.33\,kg\,h^{-1}$ (fit); $j = 3880\,A\,m^{-2}$; and $U = 0.67\,V$.

z-gradient), when the heat generation at the cool end of the active area ($x = 148$ mm) is 30% smaller and at the hot edge ($x = 40$ mm) 30% larger than the mean heat source. This means that the hottest zone in the cell is additionally heated whereas the integral heat input remains constant. The impact on the maximum temperature is small. It increases from 71.2 ° C for the homogeneous case to 72.6 ° C for the unfavorable, inhomogeneous case.

The lower limit of the error range is the result of a more favorable, yet more realistic, reciprocal heat source profile (positive z-gradient). Such a profile is closer to reality, as the high stoichiometric process air is induced to the hot side of the active area having an additional cooling effect in this sector. However, the calculated maximum temperature only decreases by 1.2 °C. Due to these small temperature variations the use of a homogeneous heat source distribution in the active area is approved.

4.2. Cooling air massflow optimization

Fig. 9 illustrates the dependency between the specific power output and the cooling air massflow. The model shows that

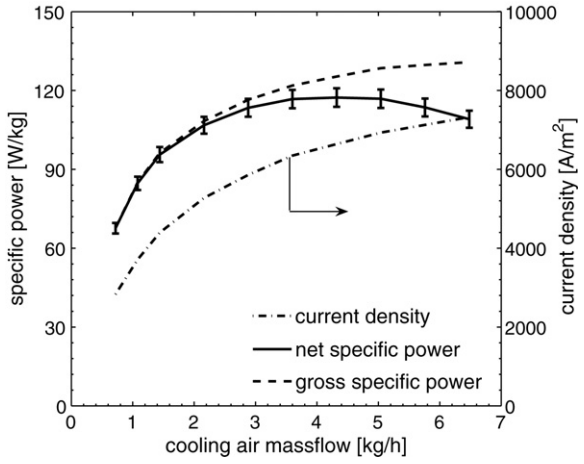

Fig. 9. Gross/net specific power and current density as a function of cooling air massflow per cell. Three percent error bar for the net specific power. Base case geometry. Fan efficiency 10%. $T_{max} = 75\,°C$.

the net specific power can be improved from 85 $W\,kg^{-1}$ for the base case to 117 $W\,kg^{-1}$ (+38%) by increasing the cooling air massflow from 1.33 to 5 $kg\,h^{-1}$ per cell. At the same time the specific cost decreases from 3.2 to 2.11 € W^{-1} (−34%). Thereby the configuration is assumed to remain unchanged. In the following this case is refered to as the massflow-optimized case.

Generally a higher cooling air massflow improves the convective cooling and the cell can operate at higher current densities. But the cooling efficiency diminishes at high cooling air massflows as the temperature difference between the cooling air and the separator plate cannot increase significantly anymore. Consequently the current density converges towards a limiting value of about 8000 $A\,m^{-2}$ for the base case. This behavior is also reflected in the gross specific power and even amplified due to a decreasing cell voltage with increasing current density. The net specific power decreases at cooling air massflows above 5 $kg\,h^{-1}$ as the power demand of the fan with an efficiency of 10% becomes significant.

The exact determination of an optimum cooling air massflow is difficult because the net specific power characteristic in the range of 3–5 $kg\,h^{-1}$ is flat. A relatively high massflow of 5 $kg\,h^{-1}$ was used for the following geometry optimization to avoid significant limitations in the convective heat removal. At the same time the parasitic load of the fan at this massflow is below 10%.

4.3. Geometry optimization

Not only the cooling air massflow but also the geometry of edge-air-cooled cells strongly influences the cooling efficiency and hence the possible maximum power output of the cell. There are two relevant parameters affecting the specific power and cost, namely the separator plate thickness and the size of active area.

The cooling channel width has a small impact. The wider the channel, the larger is the heat exchange area. However, the temperature difference at the outer edge of the channel becomes small, reducing the cooling efficiency. The cooling channel width was therefore kept constant at of 32 mm.

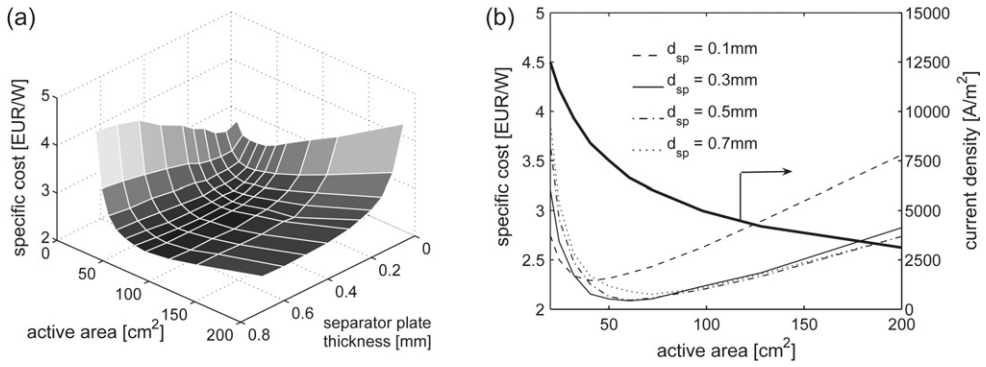

Fig. 10. (a) Specific cost surface plot over the geometry optimization field. (b) Specific cost curves as a function of active area for different separator plate thicknesses (current density is plotted for a separator plate thickness of $d_{sp} = 0.3$ mm). $T_{max} = 75\,^{\circ}$C and $\dot{m}_{cool} = 5\,kg\,h^{-1}$.

In the following the active area is used as a placeholder for the product of the flowfield width and length. Its aspect ratio has an influence on the cooling behavior. A cell with a high aspect ratio that is cooled along the long edge has a higher cooling surface and shorter heat conduction paths. On the other hand the pressure difference in the cooling channel increases and therewith the parasitic load of the fan. Apart from that a compact stack geometry was one of the initial requirements and for this purpose an aspect ratio of 2:1 was assumed to be the optimum. Calculation for an aspect ratio of 1:1 showed only a slightly worser cooling efficiency. This underlines that the aspect ratio of the cell is not a major parameter due to the high in-plane heat conductivity of the used materials.

The used cost data is geometry dependent and is composed from a fixed (e.g. periphery material, manufacturing) and a variable contribution (e.g. cell material). The used weight data is also a function of geometry and composed from a fixed and variable contribution. The fixed contributions were split to a total of 30 cells.

4.3.1. Specific cost as a function of geometry

Fig. 10 illustrates the specific cost as a function of active area and separator plate thickness. The optimum geometry in terms of specific cost is around an active area of 60 cm^2 and a separator plate thickness of 0.3 mm. However, the specific cost improvement w.r.t. the massflow-optimized case is only −1.4% (2.11–2.08 € W^{-1}) as the initial geometry was already near the optimum.

Generally the cooling of large active areas in edge-air-cooled cells is critical as long heat conduction paths are involved. Therefore to avoid exceeding the limiting temperature, the operating point of the cell has to be shifted to lower current densities as shown in Fig. 10b. This means that large active areas in edge-air-cooled cells are not well utilized. Bad utilization results in a sub-proportional increase of power with active area which is opposite to the conventional expectation for well-cooled cells. At the same time costs are strongly rising with increasing active area as the MEA represents about 80% of the stack cost and the economy of scale is marginal.

For small active areas, the effective cooling does not outweigh the high fixed cost for the periphery and the manufacturing. This raises the specific cost at small active areas even though there is no cooling limitation and the active area is well utilized. There is an optimum size of the active area in between which is in contrast to area-cooled cells, where the specific cost decreases continuously with larger active areas and with thinner plate structures.

The separator plate has almost no influence on the specific cost. This weak dependency is due to the marginal contribution of the separator plate to the total cost. Nevertheless at thicknesses below 0.3 mm the heat removal is strongly hindered and a pronounced cooling limitation occurs. As a consequence the specific cost curve for a separator plate thickness of 0.1 mm in Fig. 10b is by far the most unfavorable.

4.3.2. Specific power as a function of geometry

Beside the optimum geometry in terms of specific cost there is an optimum geometry in terms of specific power. In Fig. 11 the specific power is visualized as a function of active area and separator plate thickness. A theoretical maximum specific power of 256 $W\,kg^{-1}$ was observed at an active area of 300 cm^2 and a separator plate thickness of 0.1 mm.

The power increases sub-proportionally with increasing active area as already discussed. At the same time the cell weight grows linearly and consequently the specific power goes through a maximum. Because the active area dependency of the cell weight is rather weak, the specific power curves decrease slowly behind the maximum. At small active areas the high current densities resulting from effective cooling cannot compensate the relatively high fixed weight contributions. This maximum is in contrast to area-water-cooled stacks, where the specific power increases continuously with higher active areas.

In contrast to the specific cost, the specific power shows a strong dependency on the separator plate thickness. A thicker separator plate improves the heat removal which positively influences the power output. But at the same time the weight and the volume of the cell increases. With thinner separator plates the problem of cooling limitation becomes dominating again. Due to these two competing effects an optimum separator plate thickness of 0.1 mm is observed. However, as carbon structures with a thickness of 0.1 mm may involve difficulties with respect to mechanical integrity and handling, a separator plate thickness of 0.3 mm seems preferable.

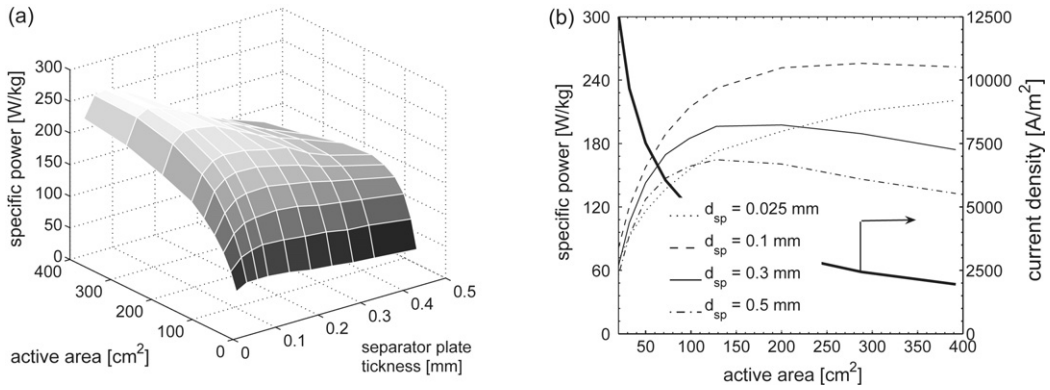

Fig. 11. (a) Specific power surface plot over the geometry optimization field. (b) Specific power curves as a function of active area for different separator plate thicknesses (current density is plotted for a separator plate thickness of $d_{sp} = 0.3$ mm). $T_{max} = 75\,^{\circ}$C and $\dot{m}_{cool} = 5\,kg\,h^{-1}$.

4.3.3. Specific cost as a function of specific power

In Fig. 12 the specific cost of Fig. 10 is plotted against the specific power of Fig. 11 for different separator plate thicknesses. Therein the different markers correspond to different active areas. An optimum for specific cost and for specific power can be distinguished. Hence edge-air-cooled cells require a trade-off between a minimum specific cost or a maximum specific power. For a separator plate thickness of 0.3 mm a minimum specific cost of 2.08 € W^{-1} can be realized with a specific power of 158 W kg^{-1}. This corresponds to a specific cost improvement of −1.4% and a specific power improvement of +24% w.r.t. the massflow-optimized case. The overall improvements w.r.t. the base case are −35% for the specific cost and +86% for the specific power. In contrast, a maximum specific power of 198 W kg^{-1} is only possible with increased specific cost of 2.58 € W^{-1} assuming the 0.3 mm limitation for the separator plate. This corresponds to an increase in specific power of +69% and an increase in specific cost of +22% w.r.t. the massflow-optimized case. The overall improvements w.r.t. the base case are +107% for specific power and only −12% for specific cost.

The distinction of two optima is in contrast to well-cooled cells, where improvements of specific power normally coincide with improvements of specific cost. In the case of edge-air-cooled cells low specific cost can only be achieved with well utilized, relatively small active areas enabling high current densities. High specific power on the other hand requires thin and light-weight plate structures resulting in cooling limitations. This increases the need for active area to obtain additional power and therefore high specific power is expensive.

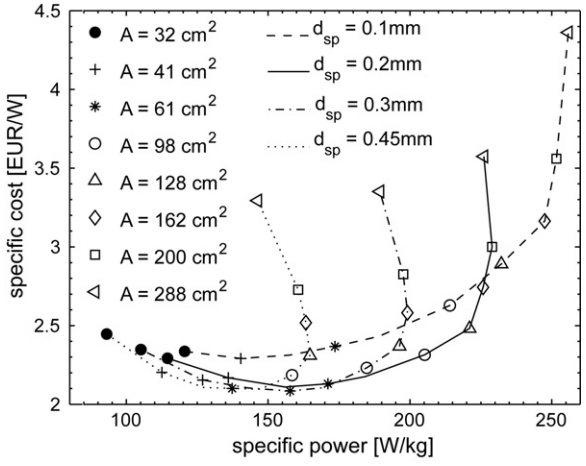

Fig. 12. Specific cost as a function of specific power for different separator plate thicknesses and active areas. $T_{max} = 75\,^{\circ}$C and $\dot{m}_{cool} = 5\,kg\,h^{-1}$.

5. Conclusions

Light-weight and low-cost PEFC stacks can be realized by using the edge-air-cooling concept. However, even when highly heat conductive materials, such as expanded graphite are used, the concepts suffer from a limited power output due to heat removal restrictions. A thermal cell model has been developed to study and quantify the thermal limitations as a function of cell geometry and current density. The model allowed for an extensive thermal analysis and the cell design was optimized with respect to maximum specific power and simultaneously minimum specific cost.

The investigation of the different cost-factors revealed that large active areas are not preferable in terms of cost. Bigger active areas have higher heat removal limitations and consequently the expensive MEA material is not well utilized. The separator plate thickness has only a strong influence on specific power. High specific power requires thin separator plates and large active areas and therefore high specific power is expensive.

Optimized edge-air-cooled cells require a trade-off between minimum specific cost and maximum specific power. For the investigated prototype system the optimization showed that with the optimal cooling air massflow, the optimal active area size and the optimal separator plate thickness an overall increase of the specific power of +86% and a simultaneous decrease of the specific cost of −35% are possible.

References

[1] U.S. Department of Energy, Hydrogen, Fuel Cells & Infrastructure Technologies Program, 2005.
[2] C. Graf, A. Vath, N. Nicoloso, J. Power Sources 155 (2006) 52–59.
[3] Y.J. Sohn, G.G. Park, T.H. Yang, Y.G. Yoon, W.Y. Lee, S.D. Yim, C.S. Kim, J. Power Sources 145 (2005) 604–609.

[4] H. Schmidt, P. Buchner, A. Datz, K. Dennerlein, S. Lang, M. Waidhas, J. Power Sources 105 (2002) 243–249.
[5] F. Büchi, J. Affolter, S. Camenzind, N. Chmielewski, P. Dietrich, M. Höckel, M. Ruge, M. Santis, Chimia 58 (2004) 869–878.
[6] F.N. Büchi, Small Size PEFC Systems for Special Applications, Handbook of Fuel Cell Technology, vol. 4, John Wiley and Sons, 2002.
[7] M. Santis, D. Schmid, M. Ruge, S. Freunberger, F.N. Büchi, Fuel Cells 4 (3) (2004) 214.
[8] A. Koschany, Cooling and Wetting Polymer-Electrolyte Fuel Cells, European Patent no. EP0968542 (1998).
[9] M. Ruge, M. Höckel, Proceedings of the 3rd European Polymer Electrolyte Fuel Cell Forum, Lucerne, Switzerland, 2005.
[10] M. Roos, E. Batawi, U. Harnisch, T. Hocker, J. Power Sources 118 (2003) 86–95.
[11] S.A. Freunberger, M. Santis, I.A. Schneider, A. Wokaun, F.N. Büchi, J. Electrochem. Soc. 153 (2006) A396–A405.
[12] E. Anderheggen, J. Korvink, M. Roos, G. Sartoris, H. Schwarzenbach, NM-SESES User Manual, 2006.
[13] H.R. Schwarz, N. Köckler, Numerische Mathematik, Teubner, 2004.